Balanced Asymmetries of Waves on the Tropopause

DAVID J. MURAKI

Courant Institute, New York University, New York, New York

GREGORY J. HAKIM

Department of Atmospheric Sciences, University of Washington, Seattle, Washington

ABSTRACT

Tropopause disturbances have long been recognized as important features for extratropical weather since they produce organized vertical motion in the troposphere. Observations of cyclonic tropopause disturbances show localized depressions of the tropopause with stratospheric values of potential vorticity extending to lower altitudes; anticyclonic disturbances are associated with comparatively smaller upward deflections of the tropopause. Analytical solutions for nonlinear interfacial wave motions are derived for an intermediate balanced dynamics based on small Rossby number asymptotics. Beyond quasigeostrophy, traveling edge-wave solutions reveal realistic asymmetries such that cyclones are associated with greater deflections of the interface, as well as larger anomalies in pressure and vertical motion compared to anticyclones.

1. Introduction

The tropopause represents an abrupt transition zone separating the well-mixed troposphere from the more stable stratosphere. As a result of the relatively strong (weak) mixing in the troposphere (stratosphere), the stratification and potential vorticity (PV) are small (large). Among the important issues related to the tropopause, some concern diabatic processes, such as the mixing between stratosphere and troposphere of mass and differing concentrations of trace chemical constituents, whereas other important issues concern adiabatic processes such as the dynamics of balanced wave motions supported by undulations in the tropopause. We are interested here in the latter concern, and are motivated by the recognition that tropopause undulations are important for extratropical weather, since these features produce organized patterns of vertical motion in the troposphere (e.g., Holton 1992, chapter 6; Bluestein 1992, section 1.9). Here we explore the steadily propagating nonlinear wave solutions supported by the tropopause under the assumptions of a uniform-PV jump at the tropopause, constant wind shear on either side of the tropopause, and small Rossby number balanced dynamics.

Observational investigations have long shown that tropopause-based disturbances are often responsible for the induction of surface cyclones (e.g., Sanders 1986; Bluestein 1992). These disturbances are described in the synoptic-meteorology literature as midtropospheric vorticity maxima, PV anomalies, and jet streaks. Some primary attributes of these disturbances are illustrated in Figs. 1 and 2, which result from a composite average of the strongest quartile of maxima (minima) in the vertical component of 500-hPa cyclonic (anticyclonic) vorticity maxima (minima) over North America during December 1988–February 1989; there are 1681 cyclonic events and 1533 anticyclonic events. Further details on the compositing method and an analysis of the cyclonic disturbances can be found in Hakim (2000). Note that qualitatively similar results are obtained by defining vorticity anomalies on the 300-hPa surface.

Plan views of potential temperature and pressure on the dynamic tropopause (defined here as the 1.5×10^{-6} m² K kg⁻¹ s⁻¹, hereafter 1.5 PVU, Ertel PV surface) illustrate an asymmetry between cyclones and anticyclones (Fig. 1). For the cyclone case, a closed contour of potential temperature and a -18 K potential temperature anomaly reflect a localized material eddy, whereas for the anticyclone case, a 12 K potential temperature anomaly accompanies a relatively broader and weaker disturbance (Figs. 1a,b). Tropopause pressure for the cyclone case reaches 480 hPa, a 168-hPa anomaly, whereas tropopause pressure for the anticyclone case reaches 230 hPa, a -67-hPa anomaly (Figs. 1c,d). Zonal cross sections further illustrate the asymmetry between cyclones and anticyclones (Fig. 2). Cyclonic

Corresponding author address: Dr. David J. Muraki, Department of Mathematics, Simon Fraser University, Burnaby, BC V5G 1S6, Canada. E-mail: E-mail: muraki@math.sfu.ca
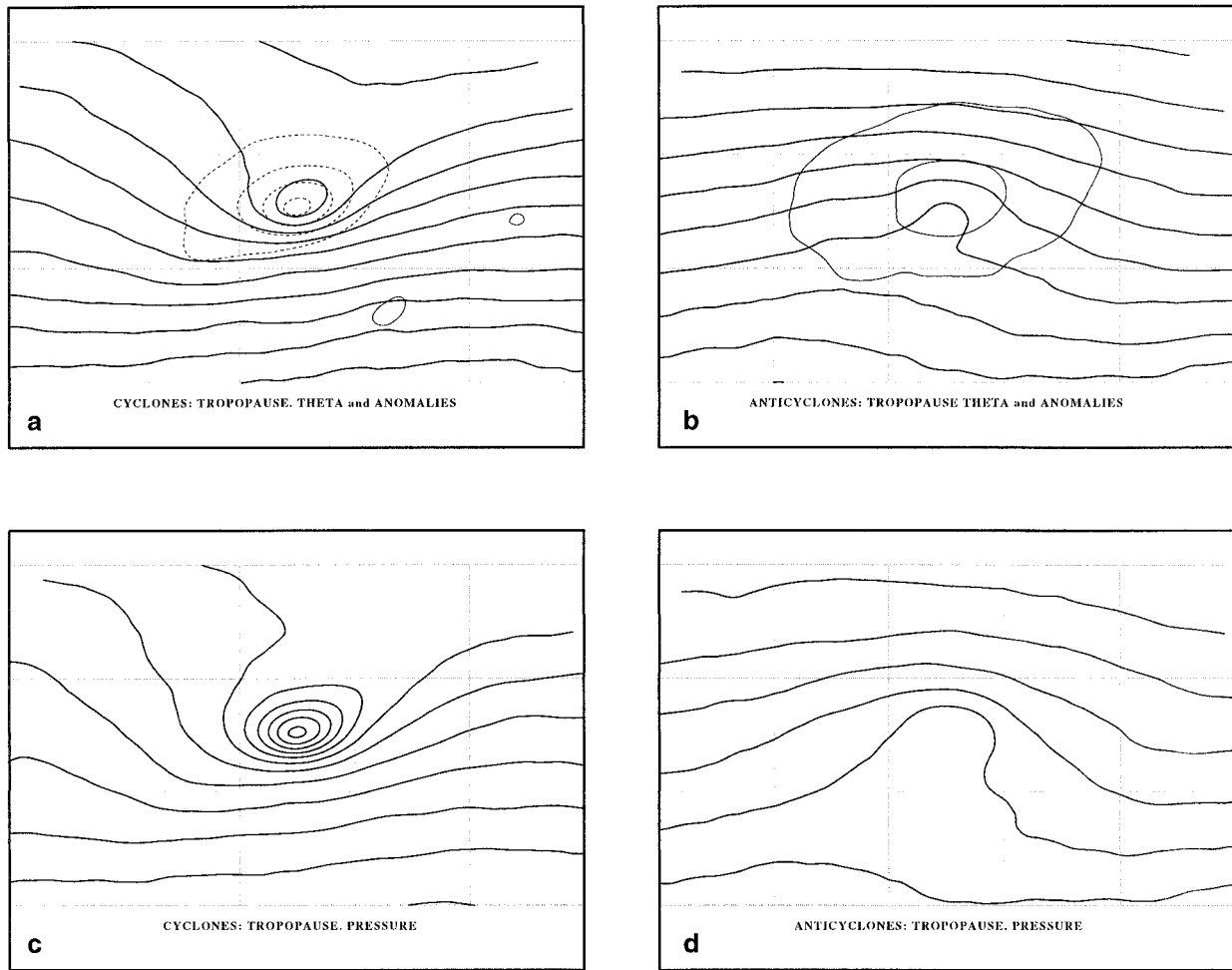
237

FIG. 1. Plan views of tropopause potential temperature (a), (b) and tropopause pressure (c), (d) for upper-tropospheric cyclones (a), (c) and upper-tropospheric anticyclones (b), (d). Mean (anomaly) potential temperature values are given by thick (thin) contours every 5 K (4 K) with negative values dashed. Pressure contours are given every 25 hPa.

disturbances exhibit a localized depression of the tropopause with stratospheric values of potential vorticity extending to lower altitude (Fig. 2a). The PV depression is flanked by a dipole of vertical motion that extends deeper into the troposphere than the stratosphere. In contrast, anticyclonic disturbances exhibit a comparatively weaker upward deflection of the tropopause and a weaker dipole of vertical motion (Fig. 2b). Meridional cross sections show that the disturbances are superposed on a gradual meridional slope to the tropopause, and the vertical motion patterns reflect the fact that the vertical circulations are tilted slightly in the zonal-height plane (Figs. 2b,d). The greatest tropopause slope is found south of the cyclonic disturbance, where the meridional gradient due to the disturbance field is in phase with the ambient gradient (Fig. 2c).

There have been two approximate treatments of the tropopause in the analytical search for balanced tropopause wave solutions. One approach treats the tropopause as a sharp transition in PV on a material surface,

such as an isentrope that crosses the tropopause; this transition is assumed independent of height. Wave solutions for this treatment address the speed and horizontal disturbance structure supported by spatially concentrated PV gradients and wind shears associated with the extratropical jet streams (e.g., Verkley 1994). A second approach treats the tropopause as a material interface separating two uniform potential vorticity fluids in the presence of vertical shear and neglects the horizontal structure of the background PV field. Wave solutions for this treatment have been found in the quasigeostrophic (QG) limit and can be interpreted in terms of the boundary edge waves of the Eady (1949) model (Rivest et al. 1992, hereafter RDF). Observational evidence of edgelike waves trapped near the tropopause has been given by Sato et al. (1993) and Hirota et al. (1995). Finally, we direct the interested reader to Juckes (1994) for a comprehensive treatment of QG tropopause dynamics.
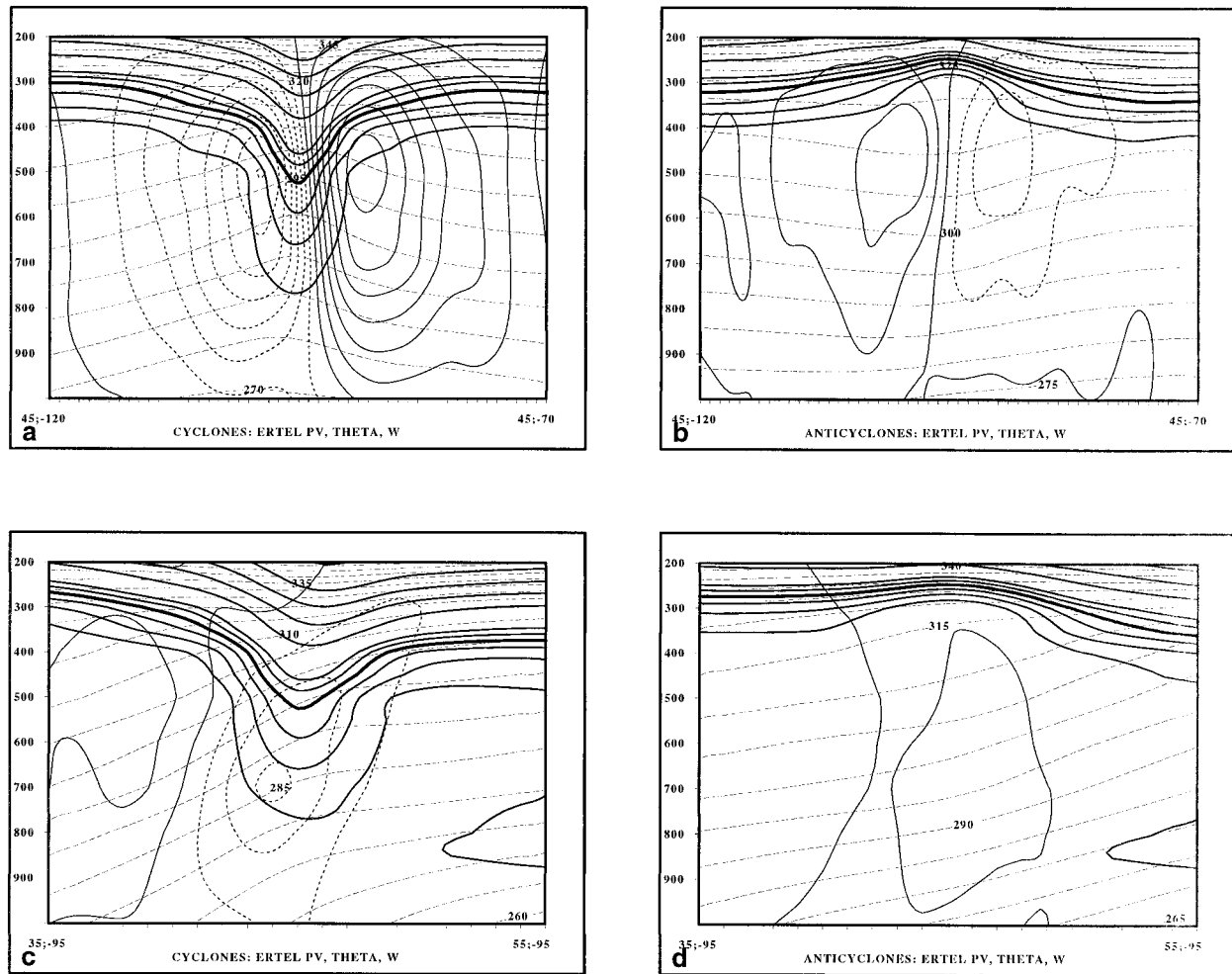
Our goal here is to uncover a theory that accounts

FIG. 2. Zonal (a), (b) and meridional (c), (d) cross sections of Ertel potential vorticity, potential temperature, and vertical motion through upper-tropospheric cyclones (a), (c), and anticyclones (b), (d). Ertel PV contours are given by thick solid lines (0.75; 1; 1.25; 1.5; 1.75; 2; 3; 4; 5; 6 PVU), and the heavy line (1.5 PVU) denotes the dynamical tropopause. Potential temperature values are given by thin lines every 5 K, and vertical motion values are given by medium lines every 0.25 Pa s^{-1} (negative values dashed). Note that 1 PVU = 10^{-6} K m^2 kg^{-1} s^{-1}.

for the prominent cyclone–anticyclone asymmetries present in tropopause observations but absent in the extant QG theory. We follow the approach of RDF and Juckes (1994) and treat the tropopause as a free material interface subject to an Eady-type shear flow. The edge-wave approach of RDF is extended to include the next-order balance effects using the QG^{+1} methodology developed in Muraki et al. (1999, hereafter MSR). The nonlinearities at next order represent the feedback of QG interfacial structure into the wave dynamics and capture the primary observational asymmetries between the interface depressions and elevations illustrated in Figs. 1 and 2. Section 2 outlines the Boussinesq primitive equations (PE), which serve as a starting point in this investigation, the reference atmosphere, and the interface conditions to be satisfied by the solutions. In section 3, the primitive equations are reformulated in terms of three QG$^+$ potentials, similar to the approach taken by MSR, and an asymptotic approximation is out-

lined. Nonlinear wave solutions are derived for flat and sloped tropopause conditions, and compared with observations in sections 4 and 5, respectively. Conclusions and opportunities for future research are described in section 6.

2. Model formulation

The formulation of the model equations proceeds in two parts. First, a set of Boussinesq primitive equations are developed for an atmosphere having uniform stratification. Second, two of these atmospheres are stacked vertically and separated by the tropopause interface; the upper layer has a stratospheric Eady base state, and the lower layer has a tropospheric Eady base state. A crucial aspect of this construction involves the proper treatment of interface conditions at the tropopause.

a. Boussinesq primitive equations

The starting point for our analysis of tropopause waves is a simple model for the midlatitude atmosphere as described by a Boussinesq equation set that also includes the inviscid, hydrostatic, and f-plane assumptions:

$$u_x^F + v_y + w_z = 0, \qquad \frac{D}{Dt}\begin{pmatrix} u^F \\ v \end{pmatrix} + f\begin{pmatrix} -v \\ u^F \end{pmatrix} = -\begin{pmatrix} \phi_x^F \\ \phi_y^F \end{pmatrix},$$

$$-\frac{g}{\theta_0}\theta^F = -\phi_z^F, \qquad\qquad \frac{D\theta^F}{Dt} = 0, \qquad (1)$$

where

$$\frac{D}{Dt} \equiv \frac{\partial}{\partial t} + u^F\frac{\partial}{\partial x} + v\frac{\partial}{\partial y} + w\frac{\partial}{\partial z} \qquad (2)$$

denotes the usual material derivative. The dependent variables are the wind velocities u^F, v, and w; the potential temperature θ^F; and the pressure ϕ^F. The superscript F indicates *full* values that include both a mean background part and a disturbance. Although the quantities ϕ^F and z will be referred to as pressure and height, strictly speaking they represent geopotential and a modified height coordinate (Hoskins and Bretherton 1972). The coefficients f, g, and θ_0 are the Coriolis parameter, the gravitational constant, and a reference potential temperature, respectively.

The tropopause represents a boundary between a low-PV troposphere and a high-PV stratosphere. This configuration can be captured by modeling the atmosphere as a two-fluid system composed of two regions of constant PV that are separated by an internal free boundary—a material interface across which the discontinuity in PV is supported. The stratospheric and tropospheric regions are distinguished by differences in their mean background states that are defined by exact Eady-shear solutions of (1). Tropopause waves are disturbance solutions from this basic Eady-shear state.

b. Eady mean reference state

The Eady mean-state atmosphere is a steady solution of the Boussinesq primitive equations (1). It represents an atmosphere having constant stratification and uniform vertical shear:

$$\phi^M \equiv \frac{1}{2}N^2z^2 - f\lambda yz - \frac{1}{2}f\lambda sy^2, \qquad \frac{g}{\theta_0}\theta^M \equiv N^2z - f\lambda y,$$

$$u^M \equiv \lambda(z + sy), \qquad (3)$$

where N is the Brunt–Väisälä frequency and λ is the shear rate. The additional parameter s is introduced in anticipation that a tilt of the $u^M = 0$ velocity surface will be useful for the construction of a two-layer atmosphere (as in RDF). In the idealized tropopause representation, the distinction between stratosphere and tro-posphere is defined through their representative values of N and λ.

c. Scaling and nondimensionalization

For disturbances upon the Eady state (3), characteristic vertical and horizontal length scales are denoted by H and L, and horizontal velocity scales by V. The assumption that the flow be near quasigeostrophic balance requires the dimensionless conditions of small aspect ratio, small Rossby number, and order-unity Burger number:

$$\delta \equiv \frac{H}{L} \ll 1, \qquad \epsilon \equiv \frac{V}{fL} \ll 1,$$

$$B \equiv \left(\frac{NH}{fL}\right)^2 = O(1). \qquad (4)$$

In addition, $O(1)$ nondimensional shear and tropopause-slope parameters associated with the background shear (3) are defined and scaled as in RDF:

$$\Lambda \equiv \frac{\lambda H}{V} = O(1), \qquad \sigma \equiv \frac{s}{\delta\epsilon} = O(1). \qquad (5)$$

Note that the viability of these scalings [(4), (5)] for QG balance demands only that the atmosphere be strongly stratified with respect to both Coriolis and shear influences ($f \ll N$ and $\lambda \ll N$).

Nondimensionalization of the Boussinesq system (1) is based on the disturbance scales x, $y \sim L$, and $z \sim H$, and on the horizontal advection timescale $t \sim L/V$. Following Pedlosky (1987), the disturbance winds and vertical motion are scaled as

$$u = u^F - u^M \sim V, \qquad v \sim V, \qquad w \sim \epsilon\delta V, \qquad (6)$$

and the pressure and potential temperature disturbance scales are those of thermal-wind balance:

$$\phi = \phi^F - \phi^M \sim VfL,$$

$$\theta = \frac{g}{\theta_0}(\theta^F - \theta^M) \sim VfL/H. \qquad (7)$$

Note that all of the disturbance variables have been carefully scaled to be independent of variations in the ambient stratification N and shear parameter λ, since these quantities are different in the stratosphere and troposphere.

d. Disturbance equations

Applying these nondimensionalizations to the Boussinesq system (1) results in the disturbance PE for the Eady mean state:

$$u_x + v_y + \epsilon w_z = 0$$

$$\epsilon \frac{Du}{Dt} + \epsilon^2 \Lambda(\sigma v + w) - v = -\phi_x$$

$$\epsilon \frac{Dv}{Dt} + u = -\phi_y$$

$$-\theta = -\phi_z$$

$$\frac{D\theta}{Dt} - \Lambda v + Bw = 0, \qquad (8)$$

where the material derivative

$$\frac{D}{Dt} \equiv \frac{\partial}{\partial t} + [\Lambda(z + \epsilon\sigma y) + u]\frac{\partial}{\partial x} + v\frac{\partial}{\partial y} + \epsilon w\frac{\partial}{\partial z} \quad (9)$$

includes advection by the Eady shear. The dimensionless expressions for the Eady state (3) with disturbances are

$$\phi^F = \frac{1}{2}\frac{B}{\epsilon}z^2 - \Lambda yz - \frac{1}{2}\epsilon\Lambda\sigma y^2 + \phi,$$

$$\theta^F = \frac{B}{\epsilon}z - \Lambda y + \theta, \qquad u^F = \Lambda z + \epsilon\Lambda\sigma y + u. \quad (10)$$

Note that the $O(1/\epsilon)$ leading terms in ϕ^F and θ^F embody the strong stratification implied by the assumption of small Rossby number. The nondimensionalized Ertel potential vorticity based on (10) is

$$Q \equiv \left[\hat{z} + \epsilon\boldsymbol{\nabla} \times \begin{pmatrix} u^F \\ v \\ 0 \end{pmatrix}\right] \cdot (\boldsymbol{\nabla}\theta^F)$$

$$= \left[\frac{B}{\epsilon} - \epsilon\Lambda(\Lambda + B\sigma)\right] + Bq, \qquad (11)$$

which is decomposed into a contribution from the Eady mean state plus a disturbance potential vorticity term denoted by q. The Eady contribution, although large, is uniform in both the stratosphere and troposphere, and provides the PV contrast primarily through a jump in the stratification B. It is also clear that only the disturbance portion of the potential vorticity (PV),

$$q = \left(v_x - u_y + \frac{1}{B}\theta_z\right)$$

$$+ \frac{\epsilon}{B}[(v_x - u_y - \epsilon\Lambda\sigma)\theta_z - v_z\theta_x + u_z\theta_y$$

$$+ \Lambda(\theta_y - u_z)], \qquad (12)$$

is dynamically relevant. Its evolution is governed by material conservation,

$$\frac{Dq}{Dt} = 0, \qquad (13)$$

and unless stated otherwise, the term PV will be reserved for this disturbance value q.

e. A tropopause atmosphere

Following RDF, the Eady basic state allows for the construction of a tropopause base state by introducing a jump in the values of Burger number B and shear Λ (and hence, a jump in PV), which supports an internal material surface. By the scalings (4) and (5), the PE (8) conveniently apply for both stratosphere and troposphere with the appropriate values of B and Λ. Stratospheric values are denoted by B_s, Λ_s and tropospheric values by B_t, Λ_t. To exploit this notational symmetry and to simplify the presentation, the bold script **s** and **t** will be omitted whenever the context is unambiguous.

For the undisturbed atmospheric state, the height of the tropopause (z_i) is located at the level with zero horizontal wind shear, $z_i + \epsilon\sigma y = 0$; see (10). The stratosphere resides above this level, $z > z_i$, and the troposphere below, $z < z_i$. Imposing continuity of the undisturbed pressure and temperature (10) at $z = z_i$, the contrast in background parameters requires

$$\sigma = \frac{\Lambda_t - \Lambda_s}{B_s - B_t}, \qquad (14)$$

which implies a unique value for the weak meridional tilt of the tropopause [cf. RDF, their Eq. (24)].

It will prove useful in the interpretation of the edge-wave dispersion relation to note that the equivalent meridional gradient in pseudo-PV (Pedlosky 1987, p. 358) of the basic state can be written as

$$\frac{\partial Q^{\mathrm{eq}}}{\partial y} = \frac{\partial^2}{\partial z \partial y}\left(\frac{\theta^F - \theta}{B}\right) \approx \left(\frac{\Lambda_t}{B_t} - \frac{\Lambda_s}{B_s}\right)\delta(z + \epsilon\sigma y), \quad (15)$$

where $\delta(z + \epsilon\sigma y)$ is the Dirac delta function acting at the tropopause. Although the tropopause slope σ becomes negative for $\Lambda_s/\Lambda_t > 1$, a negative meridional PV gradient requires the stronger condition $\Lambda_s/\Lambda_t > B_s/B_t > 1$, which reflects the considerable dynamical influence exerted by the stratification difference across the interface.

Two special reference atmospheres are considered: one having a *flat* tropopause, in the case of uniform shear ($\Lambda_s = \Lambda_t$), and the other a *sloped* tropopause, in the case without stratospheric shear ($\Lambda_s = 0$; as in RDF). Meridional profiles of full potential temperature θ^F for both reference atmospheres are shown in Fig. 3. The exact compensation by the tropopause tilt for the zero stratospheric shear is evident from the continuity of the isentropes in Fig. 3b.

f. Interface conditions

As constructed above, the reference tropopause satisfies continuity of pressure and temperature, in addition to the interface being a material surface within the shear flow. These three properties of the interface must be maintained when disturbance flow and tropopause deformation are included. The major technical difficulty
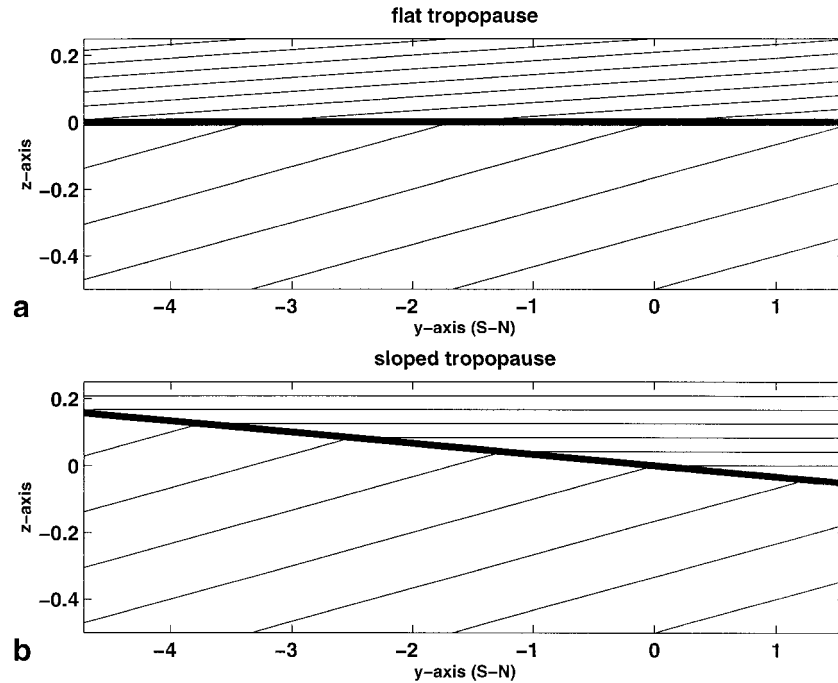
FIG. 3. Meridional cross section of potential temperature for (a) flat and (b) sloped undisturbed tropopause position. Potential temperature values are given by thin lines every 5 K. The heavy line denotes the undisturbed tropopause interface. Parameters common to both cases are $\epsilon =$ 0.1, $B_s = 4$, and $B_t = 1$. The Eady shear parameters are $\Lambda_s = 0$, $\Lambda_t = 1$ for the sloped tropopause, and $\Lambda_s = \Lambda_t = 1$ for the flat tropopause.

involves the participation of the tropopause as a dynamical surface, which distinguishes the regions of differing B and Λ in the PE (8). The equations for the interface conditions are best described in a coordinate system that naturally slopes with the undisturbed tropopause. Prior to adjusting the coordinates and outlining the interface matching conditions for the disturbed tropopause, the QG^{+1} reformulation of the PE (8) is presented.

3. QG^{+1} tropopause wave asymptotics

a. QG$^+$ reformulation of the primitive equations

The tropopause wave solutions of the disturbance PE (8), which include the next-order corrections beyond QG, are constructed following the QG$^+$ methodology, a systematic asymptotic approach to quasigeostrophic balance (MSR). This method is applied here within the context of the above PE (8), taking explicit account of the Burger number, B. The QG$^+$ method generalizes the familiar QG streamfunction representation to a three-potential representation:

$$v = \Phi_x - \frac{1}{B}G_z, \qquad -u = \Phi_y + \frac{1}{B}F_z,$$

$$\theta = \Phi_z + G_x - F_y, \qquad \epsilon Bw = F_x + G_y. \qquad (16)$$

The PE (8) are then exactly equivalent to the sequence of elliptic inversions for the potentials (Φ, F, G):

$$\nabla_B^2 \Phi = q - \frac{\epsilon}{B}[(v_x - u_y)\theta_z - v_z\theta_x + u_z\theta_y$$

$$+ \Lambda(\theta_y - u_z - \epsilon\sigma\theta_z)]$$

$$\nabla_B^2 F = \epsilon\left[-\left(\frac{D\theta}{Dt}\right)_x + \left(\frac{Dv}{Dt}\right)_z + \Lambda v_x\right]$$

$$\nabla_B^2 G = \epsilon\left[-\left(\frac{D\theta}{Dt}\right)_y - \left(\frac{Du}{Dt}\right)_z + \Lambda(v_y - \epsilon\sigma v_z - \epsilon w_z)\right],$$

$$(17)$$

where the Laplacian operator is modified by the stratification B:

$$\nabla_B^2 \equiv \frac{\partial^2}{\partial x^2} + \frac{\partial^2}{\partial y^2} + \frac{1}{B}\frac{\partial^2}{\partial z^2}. \qquad (18)$$

Inclusion of the PV evolution equation (13) completes the reformulation of the PE in terms of QG$^+$ potentials. It is emphasized that the above QG$^+$ system of equations [(16), (17), (13)] constitutes an *exact* reformulation of the disturbance PE (8). This particular form of the PE has been crafted to enable a straightforward truncation to QG and its perturbative corrections. For completeness, we note that unbalanced motions, such as gravity waves, reside within (17), and can be isolated by a judiciously chosen timescale and expansion procedure (MSR).

The QG^{+1} balanced system is constructed by assuming a perturbation solution based upon the small Rossby number (ϵ) expansion:

$$\Phi = \Phi^0 + \epsilon\Phi^1 + O(\epsilon^2), \qquad F = \epsilon F^1 + O(\epsilon^2),$$

$$G = \epsilon G^1 + O(\epsilon^2), \qquad (19)$$

which allows for an iterative inversion of correcting potentials using (17). The boundary and interface conditions for these inversions are obtained from physical conditions in terms of primitive variables. Specific to this tropopause analysis, the QG^{+1} asymptotic procedure requires an additional alteration that is dictated by the tilt of the tropopause and involves a change to a sloped coordinate frame.

b. Tropopause coordinates

The tropopause wave is obtained as a stationary wave solution in a zonally propagating frame. This wave solution must possess lateral periodicity in the directions parallel to the reference tropopause surface. With the tilted tropopause ($\sigma \neq 0$), it proves useful to express the spatial structure in terms of a (slightly) skewed coordinate system where the vertical coordinate is referenced to the undisturbed (tilted) tropopause. This motivates a change to tropopause coordinates, as defined by a translating and $O(\epsilon)$-skewed frame:

$$\overline{x} = x - ct, \qquad \overline{y} = y, \qquad \overline{z} = z + \epsilon\sigma y, \qquad \overline{t} = t, \quad (20)$$

where c is the zonal wave speed. In this moving frame, traveling wave solutions are independent of $\overline{t}$. Most important, the reference tropopause now resides at $\overline{z}_i = 0$.

c. The tropopause as a free-boundary interface

The tropopause waves are essentially two edge waves trapped on an isolated internal interface. In addition to lateral periodicity, wave disturbances are also assumed to decay in the vertical away from the tropopause $\overline{z} \to \pm\infty$. At the tropopause, the physical conditions to be satisfied are continuity of (full) pressure and temperature, and dynamics of the tropopause as a material surface.

The disturbed tropopause is described as a surface that is displaced from the reference tropopause:

$$\overline{z}_i = \epsilon h(\overline{x}, \overline{y}, \overline{t}). \qquad (21)$$

As noted in RDF and Juckes (1994), this weak $O(\epsilon)$ scaling of the tropopause displacement is a requirement for the temperature disturbances to be consistent with QG balance. Dimensionally, this means that this analysis for tropopause waves will be strictly valid only when the height of the tropopause disturbances is smaller than the Rossby height as defined by the ambient stratification. The interface continuity conditions on ϕ^F and θ^F (10), in terms of tropopause coordinates (20) can be written

$$\left\{\phi + \frac{1}{2}B\epsilon h^2\right\}_t^s = \{\theta + Bh\}_t^s = 0, \qquad (22)$$

where the bold **s**, **t** notation indicates subtraction of stratospheric and tropospheric values at the tropopause.

The third condition is that the tropopause interface represents a material surface with respect to both the upper and lower flows:

$$\left\{\frac{D}{Dt}[\overline{z} - \epsilon h(\overline{x}, \overline{y}, t)]\right\}^i$$

$$= \epsilon\{\sigma v + w - h_{\overline{t}} - (\epsilon\Lambda h + u - c)h_{\overline{x}} - vh_{\overline{y}}\}^i$$

$$= 0, \qquad (23)$$

where the superscript **i** indicates evaluation on the tropopause in either the stratosphere or the troposphere. This interface condition is required since the tropopause displacement, $h(\overline{x}, \overline{y}, \overline{t})$, is determined as part of the solution. The PE (8), or equivalently QG$^+$ (13), (16), (17), with boundary and interface conditions (22), (23) represent a complete specification of a free-boundary interface problem for the dynamics of the tropopause.

Specific to the tropopause wave, it proves convenient to combine (23) with the thermodynamic (θ advection) equation in the PE (8) to give

$$\left\{(\epsilon\Lambda h + u - c)\left(\frac{\theta}{B} + h\right)_{\overline{x}} + v\left[\frac{\theta}{B} + h - \left(\frac{\Lambda + \sigma B}{B}\right)\overline{y}\right]_{\overline{y}}\right.$$

$$\left. + \frac{\epsilon}{B}(w + \sigma v)\theta_{\overline{z}}\right\}^i = 0, \qquad (24)$$

where the restriction to a steady, $\overline{t}$-independent wave has also been made.

Finally, the weak displacement assumption ($\overline{z}_i \ll 1$) also allows the evaluation of the interface quantities that arise in the conditions (22), (24) through a Taylor expansion. For instance, the value of a function $f(\overline{x}, \overline{y}, \overline{z}, \overline{t})$ on the interface $\overline{z}_i = \epsilon h(\overline{x}, \overline{y}, \overline{t})$ has the Taylor representation

$$f(\overline{x}, \overline{y}, \overline{z}_i, \overline{t}) \sim f(\overline{x}, \overline{y}, 0, \overline{t}) + \epsilon h f_{\overline{z}}(\overline{x}, \overline{y}, 0, \overline{t})$$

$$+ \frac{1}{2}\epsilon^2 h^2 f_{\overline{z}\overline{z}}(\overline{x}, \overline{y}, 0, \overline{t}) + \cdots, \qquad (25)$$

so that all tropopause conditions can be expressed in terms of $\overline{z} = 0$ quantities. Finally, it should be noted that the formulation (21) also assumes lateral gradients of the tropopause $h(\overline{x}, \overline{y}, \overline{t})$ to be $O(1)$, which precludes the validity of this analysis for tropopause folds.

4. QG$^+$ tropopause wave solutions

Using QG theory, RDF successfully showed that a simple single-mode tropopause wave can be described using two copropagating Eady edge waves that decay away from the tropopause interface. More generally, this

QG wave corresponds to a leading-order, nonlinear solution of the PE (8) that is characterized by uniform interior PV and is steady with respect to a frame moving with speed c. In a manner similar to that of the QG^{+1} edge wave (MSR), here we derive the next-order tropopause wave solution whose nonlinear corrections display cyclone–anticyclone asymmetry.

a. QG^{+1} perturbation expansions

In tropopause coordinates, the next-order potential representations (16) are

$$v = \Phi^0_{\bar{x}} + \epsilon\left(\Phi^1_{\bar{x}} - \frac{1}{B}G^1_{\bar{z}}\right) + O(\epsilon^2)$$

$$-u = \Phi^0_{\bar{y}} + \epsilon\left(\Phi^1_{\bar{y}} + \frac{1}{B}F^1_{\bar{z}} + \sigma\Phi^0_{\bar{z}}\right) + O(\epsilon^2)$$

$$\theta = \Phi^0_{\bar{z}} + \epsilon(\Phi^1_{\bar{z}} + G^1_{\bar{x}} - F^1_{\bar{y}}) + O(\epsilon^2)$$

$$Bw = F^1_{\bar{x}} + G^1_{\bar{y}} + O(\epsilon), \quad (26)$$

which, in the flat case ($\sigma = 0$), recovers (16). In addition, the tropopause displacement is also expressed as a perturbation series:

$$h(\bar{x}, \bar{y}) = h^0(\bar{x}, \bar{y}) + \epsilon h^1(\bar{x}, \bar{y}) + O(\epsilon^2), \quad (27)$$

which allows the interface conditions (22), (24) to be satisfied expansions in Rossby number. Last, the only impact of the skewed coordinates (20) at next order in the QG$^+$ potential inversions (17) is an extra term in the Laplacian operator:

$$\overline{\nabla}^2_B = \frac{\partial^2}{\partial\bar{x}^2} + \frac{\partial^2}{\partial\bar{y}^2} + \frac{1}{B}\frac{\partial^2}{\partial\bar{z}^2} + \epsilon 2\sigma\frac{\partial^2}{\partial\bar{y}\partial\bar{z}} + O(\epsilon^2). \quad (28)$$

b. Leading-order QG tropospause wave

The leading-order wave is expressed solely in terms of $\Phi^0(\bar{x}, \bar{y}, \bar{z})$ (26) in which the potential representation (16) reduces to the familiar geostrophic relations

$$v \sim \Phi^0_{\bar{x}}, \quad -u \sim \Phi^0_{\bar{y}}, \quad \theta \sim \Phi^0_{\bar{z}}, \quad \phi \sim \Phi^0, \quad (29)$$

and Φ^0 is a solution to the zero-PV inversion (12):

$$\overline{\nabla}^2_B\Phi^0 \equiv \Phi^0_{\bar{x}\bar{x}} + \Phi^0_{\bar{y}\bar{y}} + \frac{1}{B}\Phi^0_{\bar{z}\bar{z}} = 0. \quad (30)$$

Horizontally periodic Eady solutions are single-mode upper/lower waves given by

$$\Phi^0 = \begin{cases} \mathbf{s}: & A_s \cos k\bar{x} \, \cos l\bar{y} \, \exp(-m\sqrt{B_s}\bar{z}) \\ \mathbf{t}: & A_t \cos k\bar{x} \, \cos l\bar{y} \, \exp(+m\sqrt{B_t}\bar{z}), \end{cases} \quad (31)$$

where $m^2 = k^2 + l^2$, and the sign of the exponent is chosen for decay away from the tropopause $\bar{z} \to \pm\infty$. Note that the $\mathbf{s}$, $\mathbf{t}$ solutions of Φ^0 (31) are defined by regions above and below the displaced tropopause position $\bar{z} = \epsilon h(\bar{x}, \bar{y})$.

The relative amplitudes A_s and A_t, the leading-order tropopause height $h^0(\bar{x}, \bar{y})$, and the wave speed c are determined through the interface conditions (22), (24). The weak displacement assumption permits leading-order application of the tropopause conditions at $\bar{z} = 0$, as $O(\epsilon)$ errors in the interface evaluations (25) are deferred to next order. Thus by virtue of the continuity of leading-order pressure (22), the amplitudes $A_s = A_t = A$ are the same for both upper and lower solutions. The leading-order terms of the material condition (24) can be manipulated into a zero-Jacobian condition

$$\left\{J\left[\Phi^0 + c\bar{y}, \frac{\theta^0}{B} + h^0 - \left(\frac{\Lambda + \sigma B}{B}\right)\bar{y}\right]\right\}^{\mathbf{i0}} = 0, \quad (32)$$

where $J(f, g) \equiv f_{\bar{x}}g_{\bar{y}} - f_{\bar{y}}g_{\bar{x}}$ is the Jacobian derivative; the bold **i0** superscript denotes evaluation on $\bar{z} = 0$. For a periodic wave, the Jacobian can only vanish when the two arguments are proportional. Since the nonlinearity in Jacobian (32) exactly cancels, the remaining interface conditions (32) and (22) reduce to

$$\left\{\left(\frac{\Lambda + \sigma B}{B}\right)\Phi^0 + c\left(\frac{\theta^0}{B} + h^0\right)\right\}^{\mathbf{i0}} = 0$$

$$\{\theta^0 + Bh^0\}^{\mathbf{s0}}_{\mathbf{t0}} = 0, \quad (33)$$

where the first relation is really two conditions, as it must hold at the interface for both the stratospheric and tropospheric solutions. The bold scripts **s0** and **t0** denote that the difference between stratospheric and tropospheric values are evaluated at $\bar{z} = 0$.

Quasigeostrophic solutions derive from substituting (31) into (33). The second condition in (33) gives the relationship between the interface displacement and the streamfunction,

$$h^0(\bar{x}, \bar{y}) = \frac{m}{\sqrt{B_s} - \sqrt{B_t}}\Phi^0(\bar{x}, \bar{y}, 0)$$

$$\equiv C_h\Phi^0(\bar{x}, \bar{y}, 0), \quad (34)$$

which is equivalent, for $\Lambda_s = 0$, to the corrected RDF formula noted by Juckes [1994, Eqs. (3.9) and (3.10)]. The proportionality between tropopause height and QG streamfunction, C_h, is independent of the background shear, and as expected, is singular in the limit of vanishing interface ($B_s \to B_t$). The first condition in (33) gives the dispersion relationship,

$$c = \frac{1}{m}\left(\frac{\Lambda_t}{B_t} - \frac{\Lambda_s}{B_s}\right)\left(\frac{1}{\sqrt{B_s}} + \frac{1}{\sqrt{B_t}}\right)^{-1} + O(\epsilon^2), \quad (35)$$

which again reduces to the RDF solution when $\Lambda_s = 0$. Furthermore, the direct relationship in (35) between wave speed and base-state pseudo-PV gradient (15) highlights the qualitative similarity between tropopause edge waves and classic barotropic Rossby waves. Note also that in the limit B_s or $B_t \to \infty$, (34) and (35) reduce to QG edge waves trapped on a rigid surface (Gill 1982).

The correspondences presented here are consistent with Juckes's (1994) more general observation of the dynamical equivalence between the QG tropopause and surface quasigeostrophy (Held et al. 1995). Last, although in general one might expect the wave speed c to be corrected at next order, we state here for simplicity (anticipating the QG^{+1} construction) that the correction at $O(\epsilon)$ is exactly zero.

Finally, using the thermodynamic relation, the leading-order vertical motion is given by

$$Bw^0 = [\Lambda v^0 + (c - \Lambda \overline{z})\theta_{\overline{x}}^0]$$

$$= [\Lambda \Phi^0 + (c - \Lambda \overline{z})\theta^0]_{\overline{x}}. \quad (36)$$

c. QG^{+1} wave corrections

The extension of the tropopause wave to next order in Rossby number involves solving for the potentials Φ^1, F^1, G^1 subject to the next-order interface conditions. The most important results of this calculation are the corrections that are nonlinear in the wave amplitude, as these terms are responsible for the cyclone–anticyclone asymmetries. The major complication lies in the complete solution of Φ^1, where a homogeneous boundary correction $\tilde{\Phi}^1$ must be determined. A careful statement of this difficulty is given below, and some additional details of the calculation are deferred to appendix B.

The potentials Φ^1, F^1, and G^1 are obtained by next-order Poisson inversions (17) in tropopause coordinates (20):

$$\overline{\nabla}_B^2 \Phi^1 = \frac{1}{B}\left[(\Phi_{\overline{x}\overline{z}}^0)^2 + (\Phi_{\overline{y}\overline{z}}^0)^2 + \frac{1}{B}(\Phi_{\overline{z}\overline{z}}^0)^2\right]$$
$$- \frac{2}{B}(\Lambda + \sigma B)\Phi_{\overline{y}\overline{z}}^0$$

$$\overline{\nabla}_B^2 F^1 = 2J(\Phi_{\overline{z}}^0, \Phi_{\overline{x}}^0) + 2\Lambda \Phi_{\overline{x}\overline{x}}^0$$

$$\overline{\nabla}_B^2 G^1 = 2J(\Phi_{\overline{z}}^0, \Phi_{\overline{y}}^0) + 2\Lambda \Phi_{\overline{x}\overline{y}}^0, \quad (37)$$

where extra terms in the Φ^1 equation are generated by the rotated Laplacian (28). All three potentials can be expressed almost completely in terms of derivatives and (indefinite) integrals of the QG solution:

$$\Phi^1 = \frac{1}{2B}(\Phi_{\overline{z}}^0)^2 - (\Lambda + \sigma B)\overline{z}\Phi_{\overline{y}}^0 + \tilde{\Phi}^1$$

$$F^1 = \Phi_{\overline{y}}^0 \Phi_{\overline{z}}^0 + \Lambda B \overline{z}\left(\int^{\overline{z}} \Phi_{\overline{x}\overline{x}}^0\right) + (c\theta^0 + \Lambda \Phi^0)$$

$$G^1 = -\Phi_{\overline{x}}^0 \Phi_{\overline{z}}^0 + \Lambda B \overline{z}\int^{\overline{z}} \Phi_{\overline{x}\overline{y}}^0, \quad (38)$$

with appropriate choices taken for B, Λ, and Φ^0 (31) in the stratosphere and troposphere (for notational simplicity, the formal dz is dropped from the integral operator). The final term for F^1 is a homogeneous solution,

which is necessary for QG^{+1} consistency with mass continuity (16):

$$F_{\overline{x}}^1 + G_{\overline{y}}^1 = Bw^0, \quad (39)$$

where w^0 is given by (36). At this point, it remains only to determine a homogeneous solution $\tilde{\Phi}^1$, which is necessary to satisfy the physical conditions at the interface (22), (24).

The QG^{+1} pressure is obtained from a vertical integration of the next-order hydrostatic balance $\phi_{\overline{z}}^1 = \theta^1$, where θ^1 is constructed using the QG^{+1} potentials (38):

$$\phi^1 = \Phi^1 - \frac{1}{4}\overline{\nabla}_H^2(\Phi^0)^2 - c\Phi_{\overline{y}}^0 - \Lambda \int^{\overline{z}} \Phi_{\overline{y}}^0, \quad (40)$$

and $\overline{\nabla}_H^2 = \partial_{\overline{x}}^2 + \partial_{\overline{y}}^2$.

There are two conditions that define the homogeneous contribution $\tilde{\Phi}^1$. The first condition comes from continuity of the $O(\epsilon)$ contributions of full pressure on the tropopause (22):

$$\left(\tilde{\Phi}^1 - \Lambda \int^{\overline{z}} \Phi_{\overline{y}}^0\right)_{t0}^{s0} = \frac{1}{2}(B_s - B_t)(h^0)^2, \quad (41)$$

where the apparent sign change of the right side with respect to (22) follows from the inclusion of the deferred $O(\epsilon)$ Taylor correction (25) of the leading-order pressure $\phi^0(\overline{x}, \overline{y}, \overline{z}_i)$ evaluated at $\overline{z}_i \sim \epsilon h^0$.

A second condition on $\tilde{\Phi}^1$ is given by the $O(\epsilon)$ terms of the interface condition (24). Its derivation requires a considerable amount of manipulation, and the essential details are deferred to appendix A. Specifically, for the tropopause wave (31):

$$\left\{\frac{1}{B}\left(\frac{\partial}{\partial z} + \frac{(\Lambda + \sigma B)}{c}\right)\left(\tilde{\Phi}^1 - \Lambda \int^{\overline{z}} \Phi_{\overline{y}}^0\right)\right\}_{t0}^{s0}$$
$$= (C_1\overline{\nabla}_H^2 + C_2)(\Phi^0)^2 + C_3, \quad (42)$$

where the three C constants are also defined in appendix A. Boundary conditions (41) and (42) determine a homogeneous $\tilde{\Phi}^1$ solution of the form

$$\tilde{\Phi}^1 = \tilde{\phi}_{nl}^1 + \Lambda \int^{\overline{z}} \Phi_{\overline{y}}^0 + \tilde{\Phi}_{nl}^1, \quad (43)$$

where the nonlinear part $\tilde{\Phi}_{nl}^1$ consists of a constant and second harmonics only; the full solution is given in appendix B. Note that the linear part of $\tilde{\Phi}^1$ (43) is not uniquely determined by the boundary conditions but by demanding that the solution give the QG^{+1} edge waves of MSR in the limit of either B_s or $B_t \to \infty$. Last, the correction to the tropopause displacement follows immediately from next-order continuity of potential temperature (22):

$$(B_s - B_t)h^1 = -\{\theta^1 + h^0\theta_{\overline{z}}^0\}_{t0}^{s0}, \quad (44)$$

where the second right-side term is a Taylor correction from the tropopause displacement.

TABLE 1. Values for scaling parameters, derived nondimensional quantities, and derived dimensional quantities.

Dimensional quantities		Nondimensional quantities			Dimensional scales		
L	1000 km	ϵ	$\dfrac{V}{fL}$	0.1	t	$\dfrac{L}{V}$	$\approx$27.8 h
H	10 km	δ	$\dfrac{H}{L}$	0.01	s	$\epsilon\delta\sigma$	0 or $\approx$−0.333 m km⁻¹
V	10 m s⁻¹	B_s	$\left(\dfrac{N_s H}{fL}\right)^2$	4	ϕ	VfL	10^3 m² s⁻²
f	10^{-4} s⁻¹	B_t	$\left(\dfrac{N_t H}{fL}\right)^2$	1	p	$\rho_0 VfL$	10 hPa
N_s	4×10^{-2} s⁻²	Λ_t	$\dfrac{\lambda H}{V}$	1	θ	$\dfrac{VfL}{H}\dfrac{\theta_0}{g}$	3K
N_t	1×10^{-2} s⁻²	Λ_s		1 or 0	w	$\epsilon\delta V$	1 cm s⁻¹
λ	1 m s⁻¹ km⁻¹	σ	$\dfrac{\Lambda_t - \Lambda_s}{B_s - B_t}$	0 or $-\dfrac{1}{3}$			
$\dfrac{\theta_0}{g}$	30 K s² m⁻¹						
ρ_0	1 kg m⁻³						

5. The tropopause waves

Here we discuss the structure of the tropopause wave solutions for both flat- and sloped-tropopause basic states. All figures are plotted in physical coordinates with typical dimensional values that are given in Table 1. The tropopause maps (Figs. 4–7, 10) represent a full wavelength in *y* and a half wavelength in *x*. Tropopause values are approximated at the displaced interface position using the Taylor expansion (25). In the vertical profiles (Figs. 8, 9, 10), discontinuities in the contours across the tropopause appear for two reasons. First, al-

though the interface-normal velocity is continuous at the interface, the individual wind components are unconstrained. This fact accounts for the misaligned contours of *v* in Fig. 10, and to a lesser degree *w* in Fig. 8. Second, although full temperature and pressure are continuous at the interface (22), there are systematic errors associated with the asymptotic truncation to $O(\epsilon)$ in QG and $O(\epsilon^2)$ in QG⁺¹. The tropopause wave solutions shown here, with Rossby number $\epsilon = 0.1$, are square waves with $k = l = 1$ and amplitude $A = 1.0$, except where $A = 0.7$ in Fig. 11. For simplicity, cyclone–anticyclone asymmetry is quantified below as the
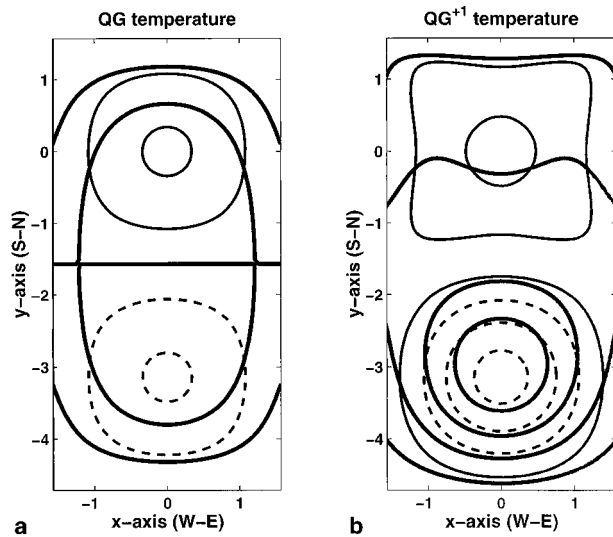

FIG. 4. Plan view of tropopause potential temperature comparing (a) QG and (b) QG⁺¹ solutions for the flat case. Full values θ^F are given by thick solid lines every 5 K, and disturbance values θ are given by thin lines every 4 K, with negative values dashed.
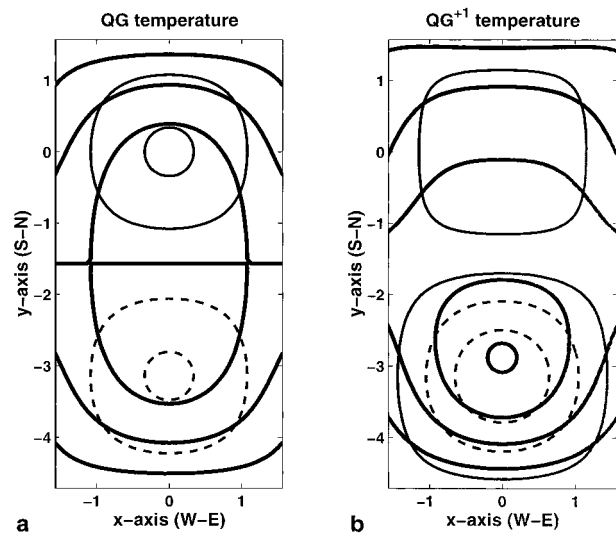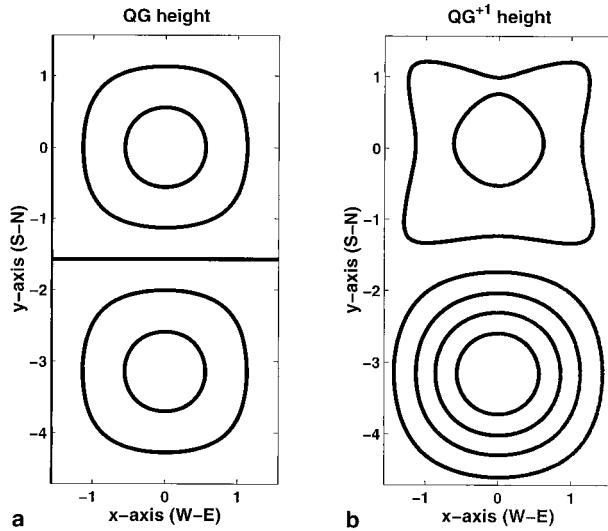
FIG. 5. Plan view of tropopause potential temperature comparing (a) QG and (b) QG⁺¹ solutions for the sloped case. Full values θ^F are given by thick solid lines every 5 K, and disturbance values θ are given by thin lines every 4 K, with negative values dashed.

FIG. 6. Plan view of tropopause height comparing (a) QG and (b) QG^{+1} solutions for the flat case. Disturbance values h are given every 500 m.

FIG. 7. Plan view of tropopause height comparing (a) QG and (b) QG^{+1} solutions for the sloped case. Full values $-\sigma y + h$ are given by thick solid lines every 600 m, and disturbance values h are given by thin lines every 500 m, with negative values dashed.

absolute value of the ratio of cyclone to anticyclone extreme values; all aspects of the QG solutions have an asymmetry ratio of unity.

The tropopause potential temperature field for the QG and QG^{+1} flat-tropopause solutions are shown in Figs. 4a and 4b. Cyclonic and anticyclonic cells are symmetric for the QG wave, whereas the cyclonic cell is notably stronger for the QG^{+1} wave, with an asymmetry ratio of 2.875. Furthermore, the contributions from the second harmonics produce a more localized, nearly axisymmetric structure for the QG^{+1} cyclone in contrast to the broader, more squarelike structure for the QG^{+1} anticyclone. The sloped-tropopause case in Fig. 5 is similar to the flat-tropopause case, except for an asymmetry of 1.89 and stronger (weaker) gradients in the full potential temperature field to the south (north) of the QG^{+1} cyclone (anticyclone). An enhanced gradient region is suggestive of upper-level fronts, which typically occur near steeply sloped regions of the tropopause (e.g., Keyser and Shapiro 1986). Two closed contours in the full potential temperature field signify a region of trapped, vortical fluid in the QG^{+1} cyclone, whereas the QG wave has open, wavelike, material contours. Comparing observations with the QG^{+1} solution shows that the QG^{+1} solution captures the qualitative properties of the cyclone–anticyclone asymmetry, as well as the material eddy and wavelike properties of the cyclone and anticyclone, respectively (cf. Fig. 5b with Figs. 1a,b).

Cyclone–anticyclone asymmetry is dramatically illustrated in the tropopause height perturbations, which have an asymmetry of 3.86 for the flat tropopause waves (Fig. 6). The height asymmetry for the sloped-tropopause solutions is 2.22, and this solution compares more favorably with observations since the ambient gradient of tropopause height is included (cf. Fig. 7b with Figs.
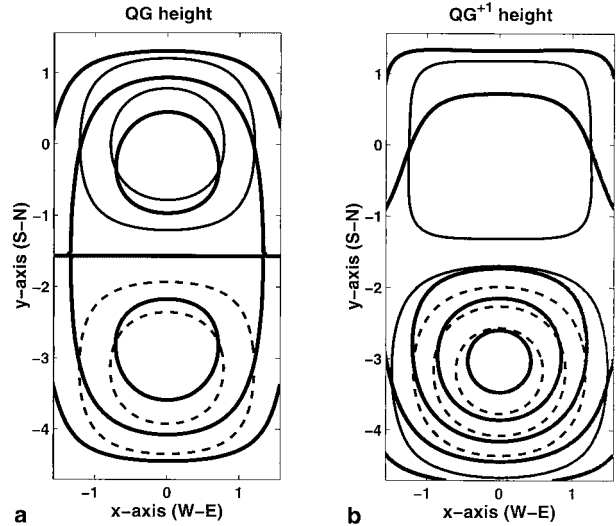
1c,d; note that tropopause pressure and height are closely correlated). Furthermore, a significant improvement in the sloped solution over the flat solution is the reduction of second-harmonic contributions in the corrections to the former, which removes a local minimum from the anomaly height field at the center of the flat anticyclone (Fig. 6b).

A zonal cross section through the waves highlights the profile of the disturbed interface, with an enhanced cyclone and a flattened anticyclone for the QG^{+1} relative to the QG solution (Fig. 8); note the qualitatively similar behavior in the observations (Figs. 2a,b). Vertical motions are damped above the interface and reach their largest magnitude *below* the interface for both QG and QG^{+1} solutions. A notable difference between the QG and QG^{+1} solutions is slightly stronger vertical motions that are concentrated toward the cyclone center in a manner similar to the dipole of vertical motion noted in observations (cf. Fig. 8b with Fig. 2a). This behavior may be explained by the dynamic interface condition, which requires greater vertical motions to elevate and depress the interface near the QG^{+1} cyclonic interface deflection. Note that since w scales with the lateral length scale as L^{-2}, solutions for higher wavenumbers k, l exhibit considerably larger vertical motions whose extrema are much closer to the interface. Since the dimensional horizontal scale of these waves is ~3000 km (half wavelength), this tendency would be more in line with the observations in Figs. 2a,b where the horizontal scale is significantly less at ~1000 km.

The potential temperature lines in the troposphere bulge upward in the cyclone and downward in the anticyclone in a manner similar to observations (cf. Figs. 8 and 2a,b), and as one would expect from PV reasoning based on local cyclonic and anticyclonic PV anomalies
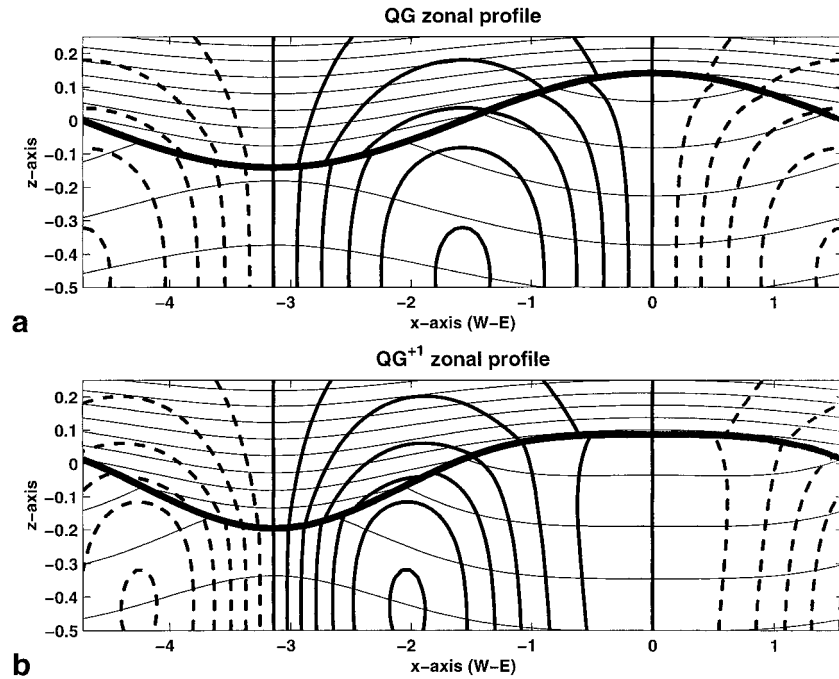
FIG. 8. Zonal cross section of full potential temperature θ^F and vertical motion w comparing (a) QG and (b) QG^{+1} solutions for the sloped case. Potential temperature is given by thin solid lines every 5 K, and vertical motion is given by thick lines every 1 mm s^{-1}, with negative values dashed. The heavy line denotes the tropopause interface.
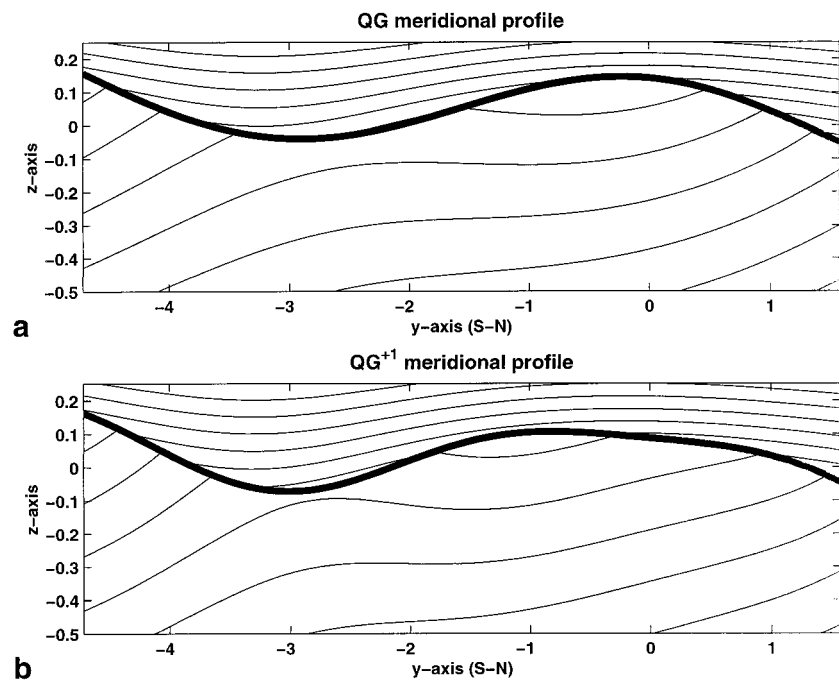

FIG. 9. Meridional cross section of full potential temperature θ^F comparing (a) QG and (b) QG^{+1} solutions for the sloped case. Potential temperature is given by thin solid lines every 5 K. The heavy line denotes the tropopause interface. The vertical motion w is identically zero in this cross section.
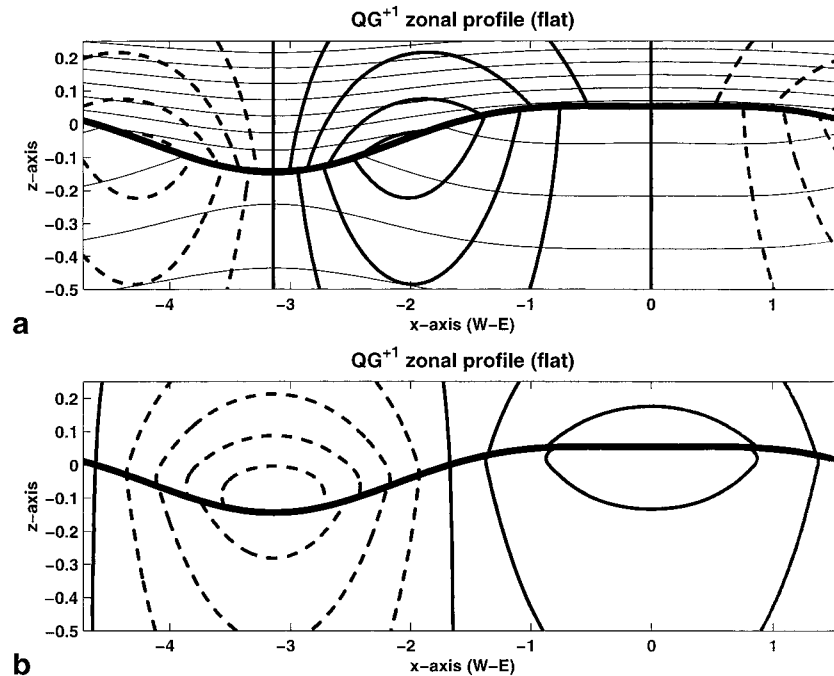
FIG. 10. Zonal cross section of (a) full potential temperature θ^F and meridional wind v and (b) disturbance pressure ϕ for the flat tropopause QG^{+1} solution. Potential temperature is given by thin solid lines every 5 K; meridional wind is given by thick lines every 2 m s^{-1}; disturbance pressure is given every 2.5 hPa (negative values dashed). The heavy line denotes the tropopause interface.

(Hoskins et al. 1985). Similar potential temperature patterns are apparent in the meridional cross section through the sloped-interface solution (Fig. 9); this cross-section orientation also illustrates the natural background slope of the tropopause (cf. Figs. 9 and 2c,d). The vertical motion w is identically zero in this profile. Note also that the tropopause slope is greatest on the equatorward portion of the cyclone and a localized wind maximum, a jet streak (e.g., Uccellini and Kocin 1987), is also found on the tropopause in this location (Fig. 11). Although the QG^{+1} analysis applies formally to small interface displacements, the solutions show an encouraging tendency toward capturing realistic properties of upper-level jet-front systems. Moreover, the QG^{+1} solution demonstrates that balanced, steadily propagating, jet streaks are possible for asymmetric vortex dipoles. These features have been documented in observations (Cunningham and Keyser 1999); however, to our knowledge, the QG^{+1} solution is the first that captures the asymmetry for Rossby-type waves.

Last, Fig. 11 shows a zonal cross section of pressure and meridional wind through the QG^{+1} flat-tropopause solution ($A = 0.7$) that serves as a basis for comparison with the idealized tropopause cyclone and anticyclone solutions of Thorpe (1986, his Figs. 1 and 2). Although the QG^{+1} solution applies to a steadily propagating square wave in a background shear, and the Thorpe vortices are steady PE solutions for specified axisymmetric distributions of tropopause potential temperature

confined above and below by rigid horizontal boundaries, the results are qualitatively similar. The greatest meridional winds are found in a dipole straddling the cyclone at the loci of maximum interface slope, and the winds decay more rapidly into the stratosphere than into the troposphere. The cyclone–anticyclone asymmetry is quite pronounced in the pressure-anomaly field, with an asymmetry of 1.73, an acorn-shaped low pressure anomaly, and an almond-shaped high pressure anomaly that compares favorably to the Thorpe results. These commonalities lend support to our conclusion that the QG^{+1} solution is capturing significant asymmetries that are present in the PE but absent in the QG equations.

6. Conclusions and future directions

The extant theory for balanced tropopause wave motions that resolve the vertical jump in potential vorticity at the interface are QG edge waves for the Eady (1949) model (Rivest et al. 1992). These waves possess a symmetry between the structure of cyclones and anticyclones. In contrast, observations show prominent asymmetries between cyclones and anticyclones associated primarily with a greater interface deflection for cyclones: larger tropopause pressure (and height) and potential temperature anomalies, and larger vertical motions near cyclones. Here we formulate an asymptotic model for tropopause wave motions and demonstrate that periodic wave solutions capture these primary
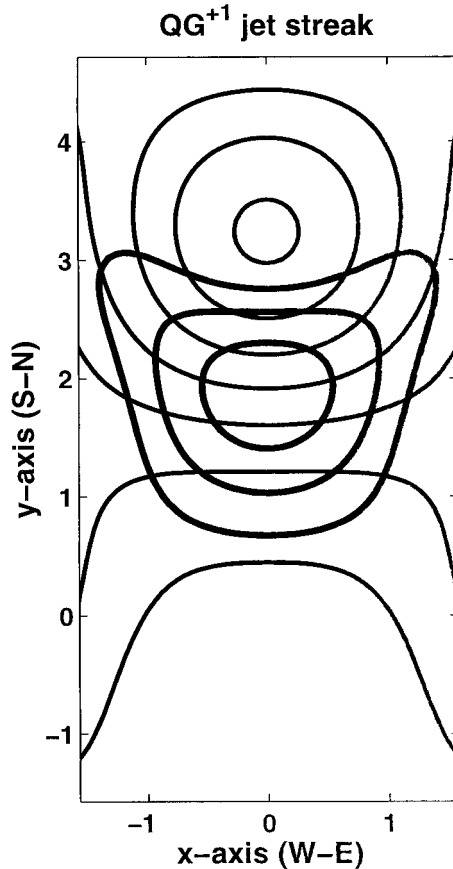
QG^{+1} jet streak

FIG. 11. Plan view of tropopause height and total wind speed for the sloped case. Full values $-\sigma y + h$ are given by thin solid lines every 600 m, and total wind speed contours are given by thick solid lines (15, 17.5, 20 m s^{-1}); a uniform background zonal wind speed of 10 m s^{-1} has been added to the solution.

asymmetries. This analysis combines an extension of the QG approximation to the primitive equations (QG^{+1}) following Muraki et al. (1999) with an expansion for the tropopause position that asymptotically satisfies continuity of pressure, temperature, and a dynamic interface condition. At leading order, the QG waves of the aforementioned extant theory are recovered. At next order, cyclone–anticyclone asymmetries emerge that compare favorably to observations. These asymmetries arise primarily due to the nonlinear feedback of QG displacements into the QG^{+1} wave dynamics, which are greatly influenced by the enhanced stability of the stratospheric base state.

Two basic states are considered: a flat tropopause associated with uniform shear in the troposphere and stratosphere, and a sloped tropopause associated with zero shear in the stratosphere. Solutions for both basic states capture the primary asymmetries noted in observations, including the larger tropopause potential temperature and height perturbations associated with cyclones. For a wave amplitude of $A = 1.0$, the contributions from just the second-harmonic corrections in

the solution produce a localized cyclonic vortex with closed material lines as compared to a broader anticyclone with square wavelike open material lines. Although vertical motions are maximal below the interface for both the QG and QG^{+1} wave solutions, the next-order corrections produce a stronger, more localized structure of vertical motion beneath the cyclone. These larger vertical motions are completely consistent with greater tropopause height deformations associated with the cyclonic part of the wave.

A noteworthy feature of the wave solution is the lack of tilt in its zonal profile despite the background vertical shear; this is consistent with the fact that a neutral (nongrowing) traveling wave cannot exchange energy with the shear flow (e.g., Pedlosky 1987, section 7.3). However, observations show a tilt of the vertical circulation in the zonal-height plane (Fig. 2a). This tilt in the observations could be due to a number of reasons, among them meridional velocity shears, time-dependent average growth (decay) of the cyclones (anticyclones), or a slight NW to SE bias of the mean jet stream.

Localized wind speed maxima, jet streaks, are captured by both the QG and QG^{+1} solutions equatorward of the cyclone disturbance. An important characteristic at next order is the cyclone–anticyclone asymmetry that is often noted in observations of jet streaks associated with vortex dipoles. A novel aspect of these next-order solutions is that the symmetry breaking to a dipole with a strong cyclone and a weak anticyclone follows naturally from a bias within the QG^{+1} dynamics.

In addition, the next-order solutions compare favorably with the primitive equation PV-inversion solutions of Thorpe (1986) for steady vortices. The close correspondence between our solutions, observations, and Thorpe's solutions supports our conclusion that the important asymmetries contained in the primitive equations are well represented within the QG^{+1} theory. This corroboration provides an incentive to conduct more careful comparisons between the solutions and observations. One opportunity would be to take these tropopause wave solutions as an initial basis for correlations between various disturbance amplitudes, such as anomalies in, for example, potential temperature, pressure, and vorticity, to compare with similar statistics obtained from observations. Another avenue for investigation would be to extract particle trajectories from these more realistic tropopause wind fields for the purpose of understanding mechanisms for vertical transport toward the tropopause.

The sloped-tropopause solution introduces the natural meridional tilt of the tropopause that is absent in the flat solutions. One apparent defect of the flat solution is a local minimum in the height anomaly field located at the center of the anticyclone; this feature is absent in the sloped solution (Fig. 7). In the sloped solution, the steepest gradients of tropopause height are found equatorward of the cyclone disturbance. This feature is associated with enhanced gradients of tropopause po-

tential temperature, and is reminiscent of an upper-level front. It has been noted that a limitation of this asymptotic model (due to the Taylor expansions used to evaluate the tropopause quantities) is that tropopause folding cannot be captured. Nonetheless, it appears that the asymmetries resolved by the sloped solutions are capturing the tendency toward such structures. Possible improvements to the tropopause dynamics might by realized by computing interface values directly through inversions obtained via a boundary-integral method, or by introducing tropopause-based coordinates. Such strategies could potentially achieve more extreme interface distortions and allow closer scrutiny of the development of upper-level fronts and tropopause folds.

The stationary nature of the tropopause wave structure presumes a state in which the dynamics are in an exact equilibrium (within the traveling frame). An important next step concerns understanding how these next-order physical effects are manifested in the time-dependent QG^{+1} dynamics of the tropopause. Of particular interest is the degree to which the dynamical asymmetries affect the development of cyclonic disturbances on the tropopause. For the case of uniform interior PV, the time-dependent version of this interfacial QG^{+1} analysis is equivalent in principle to a surface QG model (Held et al. 1995) with an additional time-dependent interface condition for tropopause displacement $h(x, y, t)$. This framework has the powerful advantage of resolving the dynamics of a three-dimensional flow in two dimensions. Furthermore, since these flows reside within a vertically infinite domain, they permit study of the interface dynamics in isolation; such isolation is impractical with current intermediate models. Potential topics of investigation with such a model include general wave dynamics, tropopause frontogenesis, shear instabilities, and turbulent evolutions. Finally, as a replacement for the rigid-lid condition in the study of baroclinic instability, this interfacial theory for a dynamical tropopause boundary offers a new framework for studying the interaction of a flexible tropopause with surface disturbances such as those that occur in the development of extratropical cyclones.

APPENDIX A

Next-Order Interface Condition

The second condition on $\tilde{\Phi}^1$ is given by the $O(\epsilon)$ terms of the interface condition (24). It is emphasized again that the weak tropopause displacement assumption allows the expression of this interface condition in terms of $\bar{z} = 0$ quantities with the evaluation on the tropopause $\bar{z}_i \sim \epsilon h^0(\bar{x}, \bar{y})$ obtained using the Taylor approximation (25). The $O(\epsilon)$ terms of (24), after considerable manipulation, take the nearly Jacobian form

$$
\begin{aligned}
&\left\{ J\left[\Phi^0 + c\bar{y}, \frac{\theta^1}{B} + h^1 + \frac{1}{B}\frac{(\Lambda + \sigma B)}{c} \right.\right. \\
&\quad \times \left(\Phi^1 + \frac{1}{2B}(\Phi^0_{\bar{z}})^2 - \Lambda \int^{\bar{z}} \Phi^0_{\bar{y}} \right) \\
&\quad \left. + \frac{\sigma}{2c^3B^2}(\Lambda + \sigma B)^2(\Phi^0)^2 \right] + (w^0 + \sigma v^0)\left(\frac{1}{B}\Phi^0_{\bar{z}\bar{z}} \right) \\
&\quad \left. + h^0 J\left[\Phi^0 + c\bar{y}, \frac{1}{B}\Phi^0_{\bar{z}\bar{z}} - \frac{1}{c}(\Lambda + \sigma B)\left(h^0 + \frac{\sigma}{c}\Phi^0 \right) \right] \right\}^{i0} \\
&= 0,
\end{aligned} \tag{A1}
$$

where the second and third terms are continuous across $\bar{z} = 0$. In the above calculation, two particularly useful identities derive from the tropopause slope σ (14) and the leading-order interface temperature (33)

$$
\{\Lambda + \sigma B\}^s_t = 0
$$

$$
\left\{ \theta^0(\bar{x}, \bar{y}, 0) + \frac{(\Lambda + \sigma B)}{c}\Phi^0(\bar{x}, \bar{y}, 0) + Bh^0(\bar{x}, \bar{y}) \right\}^i = 0. \tag{A2}
$$

Subtraction across the interface reduces (A1) to a condition on the second argument of the first Jacobian term

$$
\begin{aligned}
&\left\{ \frac{\theta^1}{B} + \frac{1}{cB}(\Lambda + \sigma B)\left(\Phi^1 + \frac{1}{2B}(\Phi^0_{\bar{z}})^2 - \Lambda \int^{\bar{z}} \Phi^0_{\bar{y}} \right) \right.\\
&\quad \left. + \frac{\sigma}{2c^3B^2}(\Lambda + \sigma B)^2(\Phi^0)^2 \right\}^{s0}_{t0} = \text{constant}, \tag{A3}
\end{aligned}
$$

where the constant is taken to be zero. Replacing θ^1 by its potential representation [(26), (37)] produces the second condition for $\tilde{\Phi}^1$ given in (42) where the constants $\mathcal{C}$ are defined as

$$
C_1 = -\frac{1}{2c}\left\{ \frac{\Lambda + \sigma B}{B} \right\}^s_t;
$$

$$
C_2 = -\frac{\sigma}{2c^3}\left\{ \frac{(\Lambda + \sigma B)^2}{B^2} \right\}^s_t = -4C_3. \tag{A4}
$$

APPENDIX B

Calculation of the Homogeneous Correction

The nonlinear part of the homogeneous solution $\tilde{\Phi}^1$ is a sum of harmonics

$$\tilde{\Phi}^1_{nl} = \begin{cases} \mathbf{s}: & \sum A_{KL} \cos K\overline{x} \, \cos L\overline{y} \, \exp(-M\sqrt{B_\mathbf{s}}\,\overline{z}) \\ \mathbf{t}: & \sum B_{KL} \cos K\overline{x} \, \cos L\overline{y} \, \exp(+M\sqrt{B_\mathbf{t}}\,\overline{z}), \end{cases}$$

(B1)

where $M^2 = K^2 + L^2$ and the sum is over the wavenumbers

$$(K, L; M) = (0, 0; 0), \ (2k, 0; 2k), \ (0, 2l; 2l),$$
$$(2k, 2l; 2m). \quad \text{(B2)}$$

The $(0, 0; 0)$-mode amplitudes involve the amplitude of the leading-order tropopause wave h^0 (34):

$$A_{00} = \frac{B_\mathbf{s}}{8} C_h^2 A^2; \qquad B_{00} = \frac{B_\mathbf{t}}{8} C_h^2 A^2;$$

$$C_h = \frac{m}{\sqrt{B_\mathbf{s}} - \sqrt{B_\mathbf{t}}}. \quad \text{(B3)}$$

The remaining second-harmonic coefficients satisfy the linear system

$$\left[\begin{array}{cc} 1 & -1 \\ \left(-\dfrac{M}{\sqrt{B_\mathbf{s}}} + \dfrac{\Lambda_\mathbf{s}}{cB_\mathbf{s}} + \dfrac{\sigma}{c}\right) & -\left(\dfrac{M}{\sqrt{B_\mathbf{t}}} + \dfrac{\Lambda_\mathbf{t}}{cB_\mathbf{t}} + \dfrac{\sigma}{c}\right) \end{array} \right] \begin{pmatrix} A_{KL} \\ B_{KL} \end{pmatrix}$$

$$= \begin{pmatrix} \mathcal{F}_1 \\ \mathcal{F}_2 \end{pmatrix}, \quad \text{(B4)}$$

where

$$\mathcal{F}_1 = \frac{B_\mathbf{s} - B_\mathbf{t}}{8} C_h^2 A^2; \qquad \mathcal{F}_2 = \frac{C_1 M^2 + C_2}{4} A^2. \quad \text{(B5)}$$

As a final comment, note that the determinant of the matrix in (B4) is zero if any of the harmonics (B1) has a vertical decay rate that matches that of the fundamental edge wave (either $2k = m$ or $2l = m$). This is the same perturbative resonance that was noted for the edge wave by MSR. The implications of this apparent singularity have yet to be understood and are the subject of current investigation.

REFERENCES

Bluestein, H. B., 1992: *Synoptic–Dynamic Meteorology in Midlatitudes.* Vol. II. Oxford, 594 pp.

Cunningham, P., and D. Keyser, 1999: The dynamics of jet streaks in the upper troposphere: Observations and idealized modelling. Preprints, *Eighth Conf. on Mesoscale Processes,* Boulder, CO, Amer. Meteor. Soc., 203–208.

Eady, E. T., 1949: Long waves and cyclone waves. *Tellus,* **1,** 33–52.

Gill, A. E., 1982: *Atmosphere–Ocean Dynamics.* Academic Press, 662 pp.

Hakim, G. J., 2000: Climatology of coherent structures on the extratropical tropopause. *Mon. Wea. Rev.,* **128,** 385–406.

Held, I. M., R. T. Pierrehumbert, S. T. Garner, and K. L. Swanson, 1995: Surface quasi-geostrophic dynamics. *J. Fluid Mech.,* **282,** 1–20.

Hirota, I., K. Yamada, and K. Sato, 1995: Medium-scale travelling waves over the North Atlantic. *J. Meteor. Soc. Japan,* **73,** 1175–1179.

Holton, J. R., 1992: *An Introduction to Dynamic Meteorology.* Academic Press, 511 pp.

Hoskins, B. J., and F. P. Bretherton, 1972: Atmospheric frontogenesis models: Mathematical formulation and solution. *J. Atmos. Sci.,* **29,** 11–37.

——, M. E. McIntyre, and A. W. Robertson, 1985: On the use and significance of isentropic potential vorticity maps. *Quart. J. Roy. Meteor. Soc.,* **111,** 877–946.

Juckes, M., 1994: Quasigeostrophic dynamics of the tropopause. *J. Atmos. Sci.,* **51,** 2756–2768.

Keyser, D., and M. A. Shapiro, 1986: A review of the structure and dynamics of upper-level frontal zones. *Mon. Wea. Rev.,* **114,** 452–499.

Muraki, D. J., C. Snyder, and R. Rotunno, 1999: The next-order corrections to quasigeostrophic theory. *J. Atmos. Sci.,* **56,** 1547–1560.

Pedlosky, J., 1987: *Geophysical Fluid Dynamics.* 2d ed. Springer-Verlag, 710 pp.

Rivest, C., C. A. Davis, and B. F. Farrell, 1992: Upper-tropospheric synoptic-scale waves. Part I: Maintenance as Eady normal modes. *J. Atmos. Sci.,* **49,** 2108–2119.

Sanders, F., 1986: Explosive cyclogenesis in the west-central North Atlantic Ocean, 1981–84. Part I: Composite structure and mean behavior. *Mon. Wea. Rev.,* **114,** 1781–1794.

Sato, K., H. Eito, and I. Hirota, 1993: Medium-scale travelling waves in the extra-tropical upper troposphere. *J. Meteor. Soc. Japan,* **71,** 427–436.

Thorpe, A. J., 1986: Synoptic scale disturbances with circular symmetry. *Mon. Wea. Rev.,* **114,** 1384–1389.

Uccellini, L. W., and P. J. Kocin, 1987: The interaction of jet streak circulations during heavy snow events along the east coast of the United States. *Wea. Forecasting,* **2,** 289–308.

Verkley, W. T. M., 1994: Tropopause dynamics and planetary waves. *J. Atmos. Sci.,* **51,** 509–529.